

Data driven discovery of human mobility models

Hao Guo^{1,2}, Weiyu Zhang^{1,2}, Junjie Yang¹, Yuanqiao Hou¹, Lei Dong^{1*}, Yu Liu^{1*}

¹*Institute of Remote Sensing and Geographical Information Systems, School of Earth and Space Sciences, Peking University, Beijing, China*

²*These authors contributed equally: Hao Guo, Weiyu Zhang.*

Email:leidong@pku.edu.cn; liuyu@urban.pku.edu.cn

Human mobility is a fundamental aspect of social behavior, with broad applications in transportation, urban planning, and epidemic modeling. However, for decades new mathematical formulas to model mobility phenomena have been scarce and usually discovered by analogy to physical processes, such as the gravity model and the radiation model. These sporadic discoveries are often thought to rely on intuition and luck in fitting empirical data. Here, we propose a systematic approach that leverages symbolic regression to automatically discover interpretable models from human mobility data. Our approach finds several well-known formulas, such as the distance decay effect and classical gravity models, as well as previously unknown ones, such as an exponential-power-law decay that can be explained by the maximum entropy principle. By relaxing the constraints on the complexity of model expressions, we further show how key variables of human mobility are progressively incorporated into the model, making this framework a powerful tool for revealing the underlying mathematical structures of complex social phenomena directly from observational data.

A deeper understanding of population movement and its underlying mechanisms is crucial for informed urban planning¹, transportation system management², and epidemic control strategies^{3,4}. Historically, the study of human mobility has evolved from qualitative description of key factors⁵ to quantitative analyses, such as the characterization of the distance decay effect⁶, culminating in formal mathematical models of population flows. The most prominent of these is the gravity model, proposed in the early 20th century^{7,8}. Analogous to Newton's law of gravitation, the gravity model posits that human mobility flows are proportional to the population of interacting locations

and inversely related to the distance between them^{9,10}.

Despite its enduring influence, progress in developing analytical models for population flows has been intermittent. Notable contributions include the intervening opportunity model^{11,12}, the radiation model¹³, and models incorporating preferential return¹⁴⁻¹⁶. However, a major obstacle to further progress within this physically-informed paradigm has been the lack of analytical frameworks derived from first principles. Unlike the physical sciences where models are often grounded in fundamental laws, social science models — particularly those describing mobility — are predominantly empirical, relying on intuition and interactive exploration to identify appropriate model forms. The inherent complexity and heterogeneity of human movement further compound this challenge.

The recent availability of high-resolution mobility data from sources such as call detail records (CDR), real-time smartphone tracking, and social media check-ins¹⁷⁻¹⁹ has offered unprecedented opportunities to investigate human mobility. These datasets provide valuable insights into both routine commuting patterns and more sporadic travel behaviors. However, the high dimensionality and inherent noise in these datasets pose substantial challenges for model identification using traditional, intuition-based approaches²⁰. This necessitates automated methods capable of leveraging large observational datasets to accelerate the discovery of accurate and generalizable models of human mobility.

Here, we introduce a machine learning-based approach for discovering models of human mobility. Specifically, we use Symbolic Regression (SR)²¹, a powerful technique that can uncover analytical expressions directly from data²²⁻³¹. Unlike traditional regression methods, SR does not assume a pre-specified function forms. Instead, it learns both the function structure and the associated parameters³². This flexibility enables the discovery of novel scientific laws³³ and provides insights into the underlying mechanisms of complex phenomena. Moreover, SR has shown the ability to produce more generalizable models than other machine learning techniques, such as neural networks^{34,35}, due to its inherent preference for simpler, more compact expressions.

We apply this approach to mobility data from three countries - China, the UK, and the US - examining both commuting and general mobility flows. Our results show that the exponential

decay gravity model consistently emerges across countries and spatial scales, suggesting its optimality in describing human mobility under certain model complexities (i.e. expression length). Beyond recovering known models, SR uncovers novel extensions, including a previously unknown exponential power-law distance decay, which can be interpreted through the maximum entropy principle³⁶. Furthermore, by analyzing symbolic models derived from flow data grouped by geographic regions, we reveal notable heterogeneity in model forms between intra- and inter-region flows, providing new insights into the diverse modes of human movement that are often masked in global models. Finally, using synthetic flow data, we validate the robustness of SR to discover various mobility models from noisy observations.

Results

Research design

To distill mathematical models of human mobility, we first compiled four large-scale datasets from three countries: 2020 cellphone data from Guangdong Province, China; 2019 cellphone data from Beijing-Tianjin-Hebei urban agglomeration, China; 2011 Census data from England; and 2011-2015 American Community Survey (ACS) data from the US (see Methods for details). These datasets encompass commuting flows (both cellphone and survey data) and general mobility patterns (cellphone data) across various spatial resolutions and geographical areas, thereby enabling a comprehensive evaluation of the robustness of potential mobility models.

Figure 1 presents the analytical framework. For each dataset, we consider four types of explanatory variables: workplace population w , residential population r , geographical distance d , and intervening opportunities s (Fig. 1b). Here, intervening opportunities represent the number of competing destinations that are closer to the origin^{13,17}. In line with the literature, we use the sum of the population in these areas as a proxy¹³. Besides variables, we consider five commonly used binary operators (Fig. 1c): addition (+), subtraction (−), multiplication (×), division (÷), power (ˆ); and two unary operators: exponentiation (exp), logarithm (ln). The goal of the SR algorithm is to identify the optimal model form by simultaneously optimizing the accuracy and complexity. Specifically, accuracy is measured by the Mean Squared Error (MSE) of the flow volumes over the

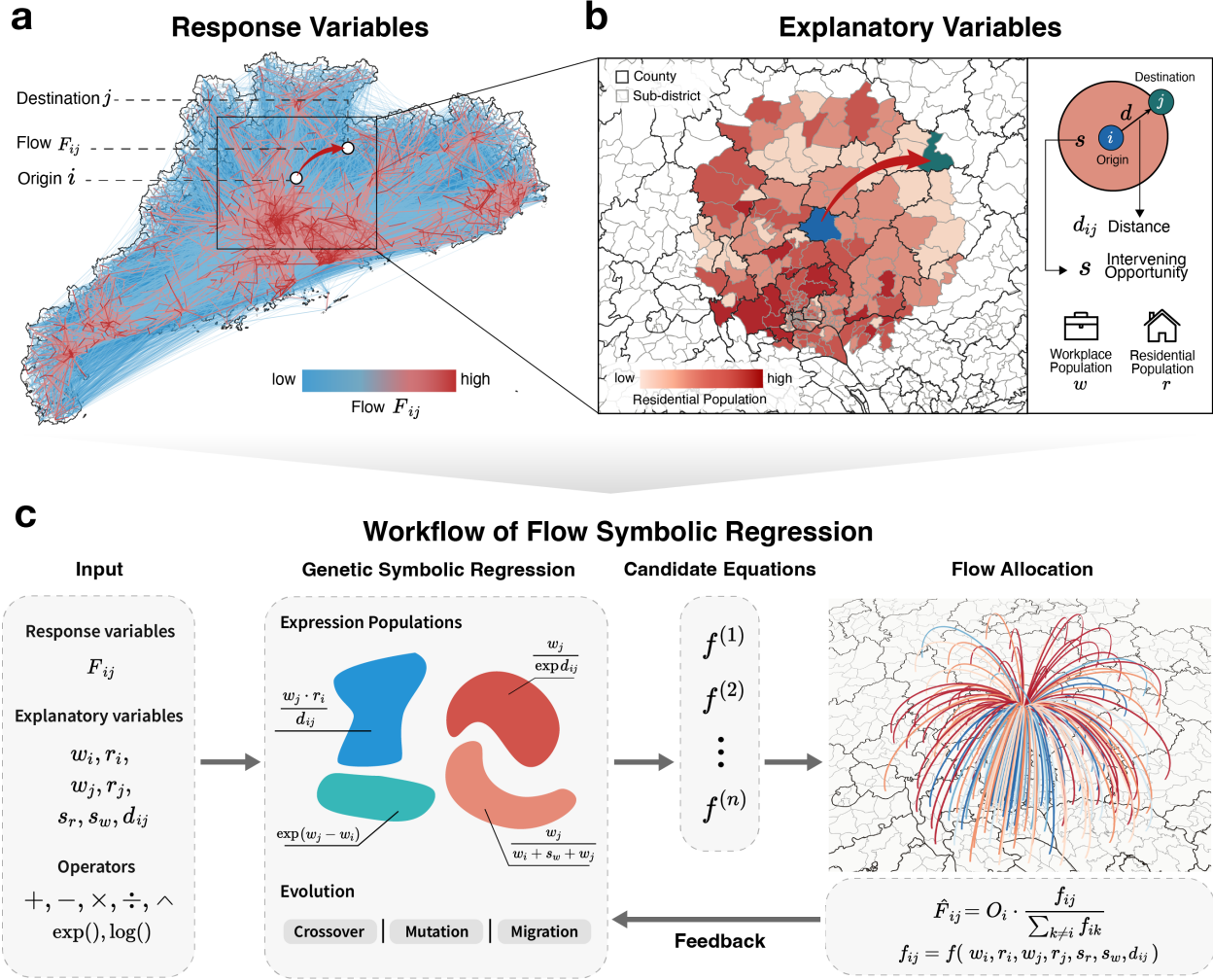


Fig. 1: The analytical framework of mobility model distillation. (a) Mobility flow of Guangdong, China. The flow volume F_{ij} from origin i to destination j is the response variable. (b) The explanatory variables include the workplace population w , the residential population r , geographic distance d_{ij} , and intervening opportunities s_w, s_r , calculated with workplace and residential population, respectively. (c) The overall workflow to automatically distill models from mobility data. Starting with response variables and explanatory variables along with seven common operators, we use a genetic-programming-based SR program to search for appropriate model forms. In each iteration, the SR program generates models for allocation weight function f . For each origin i , the total outflow O_i is allocated to each destination based on the corresponding allocation weights f_{ij} . The MSE between the allocated flow \hat{F}_{ij} and the actual flow F_{ij} is then calculated and fed back into the SR program for expression optimization.

entire dataset, while complexity is quantified by the length of the expression, defined as the total number of variables, operators, and constants, with repeated symbols counted separately²⁰. Each constant, variable, and binary operator is assigned a length of 1, while exp and ln are assigned a

length of 2 due to the implicit presence of the constant e . When the expression is represented as a full binary tree, model complexity corresponds to the number of nodes, which must always be an odd integer (see Extended Data Fig. 1 for examples).

Rather than directly modeling the origin-destination flow F_{ij} between places i and j , we model the allocation weight f_{ij} with SR. This weight is proportional to the probability that an individual starting from place i will choose destination j (Fig. 1c). Let O_i denote the total outflow from place i , F_{ij} is calculated from $\{f_{ik}\}_{k \neq i}$: $\hat{F}_{ij} = O_i f_{ij} / \sum_k f_{ik}$. This approach reduces the length of the target expression. For example, the power-law decay gravity model $F_{ij} = km_i m_j / d_{ij}^\beta$ has a complexity of 9, while its allocation weight form $f_{ij} = m_j / d_{ij}^\beta$ has a complexity of 5, where m_i, m_j are the populations of the origin i and destination j , respectively. The search space of SR grows exponentially with expression length, which can largely impact its performance on complex models. Therefore, the allocation weight approach enhances the stability and efficiency of SR.

To identify the optimal model form, we use a Genetic Programming-based SR algorithm (Fig. 1c). This algorithm evolves a population of expressions represented as trees. In analogy to natural selection, expressions with higher fitness values (calculated based on accuracy and complexity) have a higher probability of producing offspring through crossover and mutation. The algorithm generates a Pareto frontier of optimal expressions, with each expression being Pareto-optimal if no improvement in one objective (accuracy or complexity) can be made without sacrificing the other. Detailed SR settings are provided in the Methods section.

Discovering symbolic models of mobility flows

As shown in Fig. 2 and Extended Data Fig. 2, SR models achieve superior or equal accuracy to existing models of the same complexity, with existing models consistently falling on the upper-right side of the Pareto frontiers formed by the SR models (Fig. 2 a-c). Notably, at a complexity of 5, SR autonomously discovered the gravity model with exponential decay in six of the seven datasets. In the remaining case, the accuracy of the exponential decay gravity model was almost identical to that of the model on the Pareto frontier (only 1.6% higher RMSE; Supplementary Table S3). This strong convergence across diverse datasets underscores the effectiveness and parsimony of the exponential decay gravity model for representing human mobility. Consistent with previous

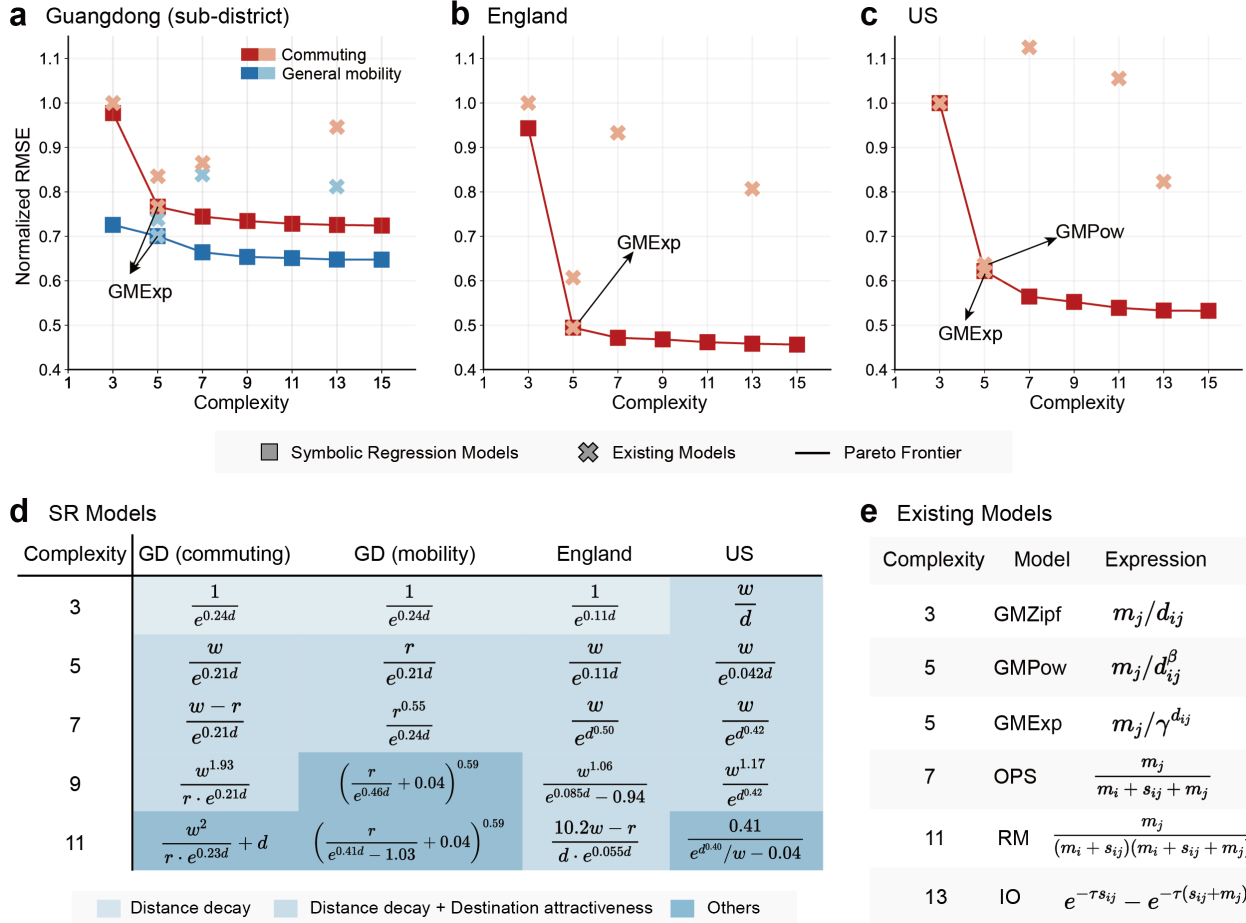
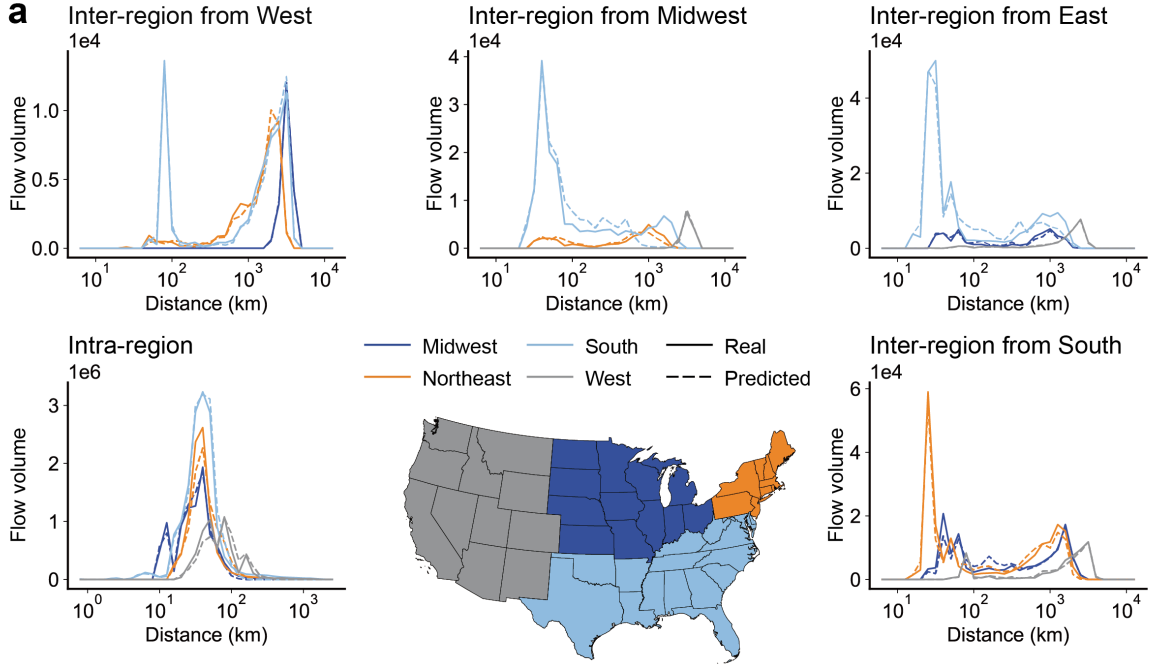


Fig. 2: SR results on mobility flow data. (a-c) Pareto frontiers of SR models on Guangdong, England, and US datasets. As flow magnitudes vary across datasets, we normalize the RMSE with that of the simplest gravity model (m_j/d_{ij}). The accuracy and complexity of six existing models are marked with crosses (note that some existing models are not shown as their errors exceed the range of the y-axis). Expressions with complexity 1 are excluded as one variable or constant is not sufficient to model the mobility flow. Across all datasets and complexity levels, the SR models consistently outperform or match the existing models in accuracy. (d) Expressions of the Pareto optimal SR models. The notations follow Fig. 1, except that d is short for d_{ij} and w, r for w_j, r_j (as origin populations are not present in these formulas). To align with existing models, some expressions are not given in the form with the lowest complexity. The distilled models are classified based on the captured effects governing human mobility. (e) Expressions of the considered existing models. GMZipf: Zipf’s simple gravity model⁸; GMPow/GMExp: gravity model with power-law/exponential decay³⁶; OPS: opportunity priority selection model³⁷; RM: radiation model¹³; IO: Schneider’s intervening opportunity model¹².

empirical analysis³⁸, the distance decay parameters of the SR-derived gravity models show a decreasing trend with the area of the spatial units, from 0.21 for Guangdong sub-districts to 0.04 for US counties (Supplementary Table S1). Theoretically, Wilson’s maximum entropy derivation of the exponential decay ($1/e^{c_{ij}}$, where c_{ij} is the travel cost from location i to j) assumes travel cost is proportional to distance (see Methods). Our empirical findings provide strong support for this theoretical interpretation: by exploring a broad space of functional forms, SR identifies the exponential decay gravity model as a near-optimal solution balancing predictive power and model simplicity. The proximity of this model to the Pareto frontier’s inflection point further suggests that the exponential decay gravity model effectively captures the distribution of flow data.

Beyond the exponential decay, SR discovered a novel distance decay function, $f(d_{ij}) = e^{d_{ij}^\alpha}$, at the complexity of 7 in both the England and US commuting datasets, with $\alpha = 0.50$ and 0.42, respectively (Fig. 2d). This new form substantially improves predictive accuracy, reducing RMSE by 4.64% in the England data and 9.23% in the US data. Within Wilson’s maximum entropy framework mentioned above, this decay form corresponds to a power-law relationship between travel cost and distance ($c_{ij} \propto d_{ij}^\alpha$, see Methods). While a linear relationship is commonly assumed in transportation research, the relationship between travel cost (including monetary and time cost) and distance can be complicated by mixed transportation modes, leading to different function forms³⁹. Our finding provides a new hypothesis for empirical validation in the future. Regardless, the improved predictive performance of this interpretable decay function highlights its potential for future applications in human mobility modeling.

Regarding the other existing models, the gravity model with power-law decay is second best overall, with an average 11.2% higher RMSE than the exponential decay (Extended Data Table 1). Models based on intervening opportunity do not perform well on most datasets. On average, the RMSE of the radiation model is 92.0% higher than the SR model with the same complexity, and the error increase for Schneider’s intervening opportunity model and opportunity priority selection model are 39.8% and 49.1%, respectively. Besides, the intervening opportunity appears in the Pareto optimal SR models on only one of the seven datasets. Hence, we found no evidence that the intervening opportunity better describes the decay effect than geographic distance.



	Midwest	Northeast	South	West	Contiguous US
Midwest	$w_j/e^{0.073d}$	$(\log d)^{-14.7}$ $(w_j/d^{4.02})$	$w_j/d^{4.57}$	$w_i w_j + d$ $(w_j/d^{1.85})$	$w_j/e^{0.072d}$
Northeast	$w_j/s_w^{1.64}$ $(w_j/d^{4.41})$	$w_j/e^{0.042d}$	$w_j/d^{2.87}$	$(w_j + 85.7)/d$ $(w_j/d^{2.73})$	$w_j/e^{0.042d}$
South	$w_j/(w_i + s_w)$ $(w_j/d^{3.16})$	$w_j/d^{2.85}$	$w_j/e^{0.056d}$	$d/(s_w + 0.15)$ $(w_j/d^{3.31})$	$w_j/e^{0.056d}$
West	$w_j^{0.004w_i}$ $(w_j \cdot d^{1.81})$	$w_j^{0.38}/d$ $(w_j/d^{2.73})$	$0.64^{s_w} + 0.005$ $(w_j/d^{2.30})$	$w_j/e^{0.018d}$	$w_j/e^{0.018d}$

Comparison with the gravity model ■ More accurate ■ Less accurate ■ Consistent

Fig. 3: Spatial heterogeneity of the mobility model across US. (a) The distance distribution of commuting flows, grouped by geographic regions. The predicted flows are from the complexity 5 SR model on each subset grouped by the origin and destination region. For inter-region flows, each subplot shows outflows from one region, and the line color corresponds to the destination region. (b) SR models at complexity 5 for commuting flows. Each row/column represents the region containing the residential/work place. The notations in formulas are the same as in Fig. 1. The accuracy of these models is compared with one of the power-law and exponential gravity models which produces lower error on the subset of flow data. A red/blue cell indicates the accuracy of the SR model is better/worse (measured with RMSE); in such cases, the gravity model is given in parentheses. A grey cell means the SR model is identical to the gravity model.

Geographical heterogeneity of mobility models

Given the nature of spatial heterogeneity, the global modeling approach discussed above may represent merely the average generation process of human mobility, ignoring possibly important spatial disparities^{40–42}. To investigate the consistency of mobility models across geographical areas, we partition the US commuting flow data according to the four regions (Northeast, Midwest, East, and West; Fig. 3a), resulting in 4 intra-region subsets and 12 inter-region subsets, and independently apply SR to each subset. Other SR settings are consistent with the analysis at the whole country level.

For all four subsets of intra-region flows, the exponential decay gravity model remains optimal as suggested by SR (the diagonal expressions in Fig. 3b). This provides the basis for the model’s overall optimality as intra-region flows dominate commuting flows, containing 97.5% of flow volumes. Yet the exponential decay gravity model appears to be suboptimal for inter-region commuting. Over the 12 subsets of inter-region flows, the power-law decay gravity model consistently outperforms exponential decay. Moreover, even better models are discovered by SR in 7 of the 12 subsets.

This disparity in optimal model form may indicate difference in the mechanisms governing inter-region and intra-region commuting. Actually, the distance distribution of intra-region flows follow a typical distance decay pattern, while uncommon bimodality is observed for inter-region subsets, with a long-range peak at around 1000 km (Fig. 3a). Through examination of the flow data, we find the destinations of these flows are mostly large cities, with the top 5 destinations as Chicago, New York, Los Angeles, Houston, and Dallas. We speculate that, with more job opportunities, the attractiveness of these large cities may be much stronger than the distance friction effect in long-distance commuting, leading to weak or even disappeared distance decay. This difference is also reflected in some SR models for inter-region commuting, where flow volumes do not decrease with distance as usual (e.g. models for flows between Midwest and West in Fig. 3b).

Stability of Symbolic Regression under noise

All observational data contain noise, and if the noise is high enough, it is likely that we will not

be able to identify valid information or models⁴³. To evaluate the effectiveness of SR in the face of noisy mobility data, we conducted experiments on synthetic data (since the noise distribution in the real data is unknown). Specifically, we align the settings with our analysis on US data. Using the real spatial boundary, workplace population, and total outflow, we generate origin-destination flows based on three mobility models: the exponential decay gravity model, the power-law decay gravity model, and radiation model. We generated five samples of flow data at each of 9 noise levels (additive Gaussian noise with the standard error σ increasing from 0 to 2.0 with a step of 0.25), where the middle level ($\sigma = 1.0$) is comparable to the amount of random noise in real data (see Methods). The SR program was independently applied to each sample.

Figure 4 reports the number of successful instances where SR discovers the correct form of the generation model. When no random noise is applied, all three models can be successfully distilled. Furthermore, under a moderate amount of noise (below $\sigma = 1.0$), SR still discovers the two gravity models with 100% success rate, while the discovery of the radiation model becomes unstable as the noise level increases (Fig. 4). The latter, however, does not imply that SR produces sub-optimal models. In most cases, the SR models with complexity 11 actually have better accuracy than the radiation model, which indicates the model that best describes the data has changed because of the noise introduced. Such “shifted” formulas discovered by SR are inconsistent across samples. Some of them resembles the radiation models, such as $w_j/(w_i + s_w + aw_j)^\beta$, $w_j^\alpha/(w_i + s_w + a)^\beta$, $w_j/(w_i + s_w)(w_i + as_w)$, where a, α, β are constants. These results suggest ways to extend the radiation model by introducing parameters to better model noisy data.

Discussion

Automatic distilling symbolic models from social data can be more challenging than from physical data, as human behavior is difficult to measure with explicit expressions. In this work, we show that SR is capable of discovering accurate and compact models that capture the regularities in human mobility, and the derived Pareto optimal models reveal feasible ways to extend the basic gravity formula, some of which are previously unknown. More generally, the accumulation of observational data and the progress in symbolic regression provide a promising way to build

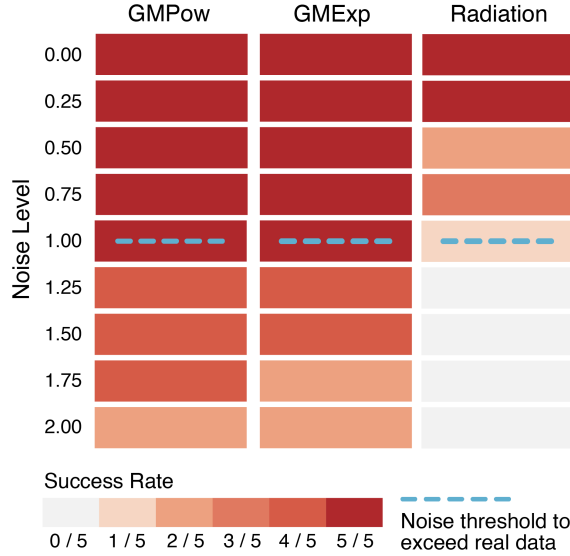


Fig. 4: The success rate of SR to reproduce generation models on simulated data. The additive Gaussian noise on the logarithm of flows is applied, with the minimum noise level to exceed real data (measured by model CPC) marked. Symbolic regression remains robust to random noise. Only at relatively high levels of noise do three generation models fail to be successfully discovered by symbolic regression.

empirical models in the social sciences. Rather than comparing the accuracy of existing candidate models, SR allows us to answer the questions: Does an existing model have the best form among all possible expressions, given a set of operators? If not, does SR suggest new candidate models of theoretical interest? In the future, it is intriguing to apply SR to more location features other than population for mobility model discovery. We also look forward to applications of SR beyond mobility data, which may provide new perspectives on the quantitative modeling of social phenomena.

We gain insight into human mobility from not only the SR-derived explicit mathematical models, but also how key factors are progressively incorporated as the allowed model complexity increases. As shown in Fig. 2d and Extended Data Fig. 2c, SR first captures the distance friction effect—near destinations attract more people than distant ones—at complexity 3, suggesting it is the principal effect governing human mobility. Another key factor revealed by SR is the destination attractiveness (represented by population), which is mostly incorporated into the models at complexity 5. Places with larger populations tend to attract more mobility flows, as they

provide a greater number and diversity of goods, services, and job opportunities. Most SR models at complexity 7 and 9 share the form of $g(w_j, r_j)/f(d_{ij})$, which still combine the destination attractiveness and the distance friction effect, yet with more complex function forms for one or both effects. As complexity further increases, the SR models become inconsistent across datasets and difficult to explain. These models are not likely to be general models for mobility flows, but capturing the characteristics of a single dataset.

Our analysis also reveals the limitations of Genetic Programming-based SR. Although the performance of SR on simple formulas (complexity < 9) is generally satisfactory, the derived formulas for longer expressions are inconsistent across repeated runs, indicating that sub-optimal solutions are found. This may be due to the exponentially growing search space. Existing literature also points out that SR is only robustly applicable to datasets with fewer than 10 variables²⁵. Incorporating neural networks and symbolic regression might be a feasible approach to discover more complicated models. For example, SR could be applied to separable modules of a neural network, and the distilled formulas are then combined into a complete expression^{29,44,45}. Future studies could investigate the effectiveness of such neuro-symbolic approaches for knowledge discovery in the social sciences.

Methods

Empirical data. The Guangdong dataset is provided by China Mobile Communications Corporation, the largest telecommunications operator in China. The raw dataset comprises individual movement trajectories of 5 million users in November 2020, with a spatial resolution of $500\text{ m} \times 500\text{ m}$. For the mobility flow dataset, individual movements are aggregated at the sub-district and county levels based on the grids' center locations. For the commuting flow dataset, an individual's home is defined as the location where they stayed the longest between 12:00 AM and 7:00 AM, while the workplace is defined as the location where they stayed the longest between 9:00 AM and 6:00 PM. Commuting flows are identified based on movements from the home location to the workplace in the morning (before 12:00 PM). Subsequently, commuting movements are aggregated similarly to the mobility flow dataset. The residential / workplace populations are derived based on the number of residents and workers within each spatial unit.

The Beijing-Tianjin-Hebei mobility data is provided by China Unicom, which contains aggregated inter-county mobility from November 4 to 10, 2019. The population data in 2019 are collected from official statistical yearbooks.

The commuting datasets in England and the Contiguous US record the location of usual residence and place of work of employed residents, aggregated to MLAD and county levels, respectively. The sources of residential and workplace population data are the same as the flow data (2011 Census for England, and 2011-2015 ACS 5-year estimate for US).

For all datasets above, we only consider flows between spatial units, so flows with the same origin and destination are removed. Moreover, the intervening opportunity is based on the population data at finer scale [Middle layer Super Output Area (MSOA) in England, sub-district in Guangdong]. The number and size of spatial units, as well as the number of observations (origin-destination pairs) of each dataset, are given in Supplementary Table S1. The mobility flows are visualized in Extended Data Figs. 3-7. For calibration of existing models, workplace populations are used on commuting datasets for better accuracy than residential populations, while only residential populations are available for mobility datasets.

Simulated data. We introduce random noise on model-generated flows to represent factors of mobility which are not captured by the symbolic models. We apply additive Gaussian noise on the logarithm of flows, which ensures the flows are non-negative. Assume \bar{T}_{ij} is the model-generated flow from place i to j , the synthetic flow T_{ij} is sampled as

$$T_{ij} = \bar{T}_{ij} \exp(\epsilon), \epsilon \sim \mathcal{N}(0, \sigma^2) \quad (1)$$

where $\mathcal{N}(0, \sigma^2)$ is the Gaussian distribution with mean zero and variance σ^2 . We do not consider a simple additive Gaussian noise for potential heteroskedasticity, as the variation of large and small flows are not likely to be the same. To align with real data, we rounded T_{ij} to the closest integer. Flows less than 3 are removed for symbolic regression.

To compare with the potential noise level in the real data, we use Common Part of Commuters (CPC)⁴⁶ to measure the discrepancy between the model-predicted flows and real flows. As a common metric for flow prediction, CPC is defined as:

$$\text{CPC} = \frac{2 \sum_{i,j} \min\{F_{ij}, \hat{F}_{ij}\}}{\sum_{i,j} F_{ij} + \sum_{i,j} \hat{F}_{ij}} \quad (2)$$

where F_{ij}, \hat{F}_{ij} are the real and predicted flow volume from place i to j , respectively. The range of CPC is $[0, 1]$, and lower value indicates a worse match between real and predicted flows, hence higher level of random fluctuation. Using CPC of the exponential decay gravity model on US data (0.728) as a threshold, we identify the minimum noise level in simulated data where the CPC of the generation model falls under 0.728, which is $\sigma = 1.0$ for all three considered generation models (Fig. 4).

Symbolic Regression. Given a set of functions \mathcal{P} , a dataset $\{\mathbf{x}_i, y_i\}_{i=1}^n$. Assume $\mathcal{L} : \mathbb{R} \times \mathbb{R} \rightarrow [0, \infty)$ is a distance function, where common choices are squared error or absolute error; C is a measure of function complexity. Symbolic regression (SR) may be formulated as a minimization problem to find

$$f^* \in \arg \min_{f \in \mathcal{F}} \frac{1}{n} \sum_{i=1}^n \mathcal{L}(y_i, f(\mathbf{x}_i)) + \lambda C(f) \quad (3)$$

where \mathcal{F} is the set of functions which can be formed by composition of the functions in \mathcal{P} ; λ is a penalty factor for complexity. In practice, SR is often solved as a multi-objective optimization

problem which jointly minimizes the fitting error and the model complexity²⁰. SR is proven to be NP-hard⁴⁷, which indicates an exact and efficient solution might not exist. Though methods based on physical principles^{48,49}, neural networks^{50–52}, and Bayesian computation^{53,54} are emerging recently, genetic programming^{32,55,56} remains the mainstream approach to SR.

We utilize the Julia package `SymbolicRegression.jl`²⁰ as it is specially designed for symbolic regression on scientific data. Several enhancements to the general framework of genetic programming are implemented, including the integration of simulated annealing, age-regularization to avoid premature convergence, expression simplification and constant optimization, a modified loss to balance expression optimization at all complexity, and migration of expressions between several parallel populations. The output contains all Pareto optimal expressions regarding accuracy and complexity. We refer to²⁰ for technical details. Nevertheless, optimization of the allocation weight function is not readily supported by the package. We develop our SR program by modifying the evaluation function in `SymbolicRegression.jl` to calculate flow volumes from allocation weights. As constant optimization only takes place with probability in the genetic search process, we also add a constant optimization step before the output of final expressions.

Due to the randomness of the genetic algorithm, we repeat the SR procedure multiple times for each dataset. Typically, we first use all features as explanatory variables, then restrict the set of variables to those shown to be important. Fewer variables lead to a smaller search space, thus may yield better solutions. The number of iterations is set as 100 throughout this study. Batching is necessary to accelerate the program for large flow datasets. By default, the Broyden-Fletcher-Goldfarb-Shanno (BFGS) algorithm is used to optimize constants, and the Nelder-Mead algorithm is used if the former fails. The Pareto optimal expressions within the combined output of repeated runs are selected as final models. The detail of SR settings on each dataset is given in Supplementary Table S2.

Maximum entropy approach to the gravity model. Inspired by statistical mechanics, Wilson applied the concept of entropy on origin-destination flow data, and deduced the gravity model using the maximum entropy principle³⁶. Let F_{ij} denote the flow from place i to j , the entropy of a

flow distribution $\{F_{ij}\}$ is defined as

$$S = - \sum_{i,j} p_{ij} \ln p_{ij} \quad (4)$$

where $p_{ij} = F_{ij} / \sum_{i,j} F_{ij}$. Here the entropy is approximately linear to the logarithmic number of “microscopic states” of the system (a microscopic state contains a full description of the origin and destination of each person), hence the distribution $\{F_{ij}\}$ with maximum entropy corresponds to the most probable “macroscopic state”.

Consider the following constraints on mobility flows:

$$\sum_j F_{ij} = O_i, \forall i \quad (5)$$

$$\sum_i F_{ij} = D_j, \forall j \quad (6)$$

$$\sum_{i,j} F_{ij} c_{ij} = C \quad (7)$$

where c_{ij} denote the travel cost from place i to j . The first two constraints ensure the distribution is consistent with the total outflow and inflow of each place. The last constraint asserts that human mobility is restricted by travel costs. Using the method of Lagrange multipliers to maximize S given the constraints above, we get the doubly-constrained gravity model as follows:

$$F_{ij} = A_i B_j O_i D_j e^{-\beta c_{ij}} \quad (8)$$

where $A_i = \left(\sum_j B_j D_j e^{-\beta c_{ij}} \right)^{-1}$, $B_j = \left(\sum_i A_i O_i e^{-\beta c_{ij}} \right)^{-1}$. This form suggests that flow volumes follow an exponential decay with travel cost. The decay parameter β arises from the unknown total cost C , and usually needs real data to be calibrated. The decay function of distance can be deduced by substituting the relationship between travel cost and distance. For example, given $c_{ij} = k d_{ij}$, we get the exponential decay $e^{-k\beta d_{ij}}$; given $c_{ij} = k \ln d_{ij}$, we get the power-law decay $d_{ij}^{-k\beta}$. Therefore, the discovered exponential-power decay $e^{-d_{ij}^\alpha}$ indicates a power-law relationship between travel cost and distance $c_{ij} = \frac{1}{\beta} d_{ij}^\alpha$.

References

1. Abbiasov, T. *et al.* The 15-minute city quantified using human mobility data. *Nature Human Behaviour* **8**, 445–455 (2024).
2. Çolak, S., Lima, A. & González, M. C. Understanding congested travel in urban areas. *Nature Communications* **7**, 10793 (2016).
3. Jia, J. S. *et al.* Population flow drives spatio-temporal distribution of COVID-19 in China. *Nature* **582**, 389–394 (2020).
4. Santana, C. *et al.* COVID-19 is linked to changes in the time–space dimension of human mobility. *Nature Human Behaviour* **7**, 1729–1739 (2023).
5. Ravenstein, E. G. The laws of migration. *Journal of the Statistical Society of London* **48**, 167–235 (1885).
6. Lill, E. Die grundgesetze des personenverkehrs. *Zeitschrift für Eisenbahnen und Dampfschifffahrt der Österreichisch-Ungarischen Monarchie* **35**, 697–706 (1889).
7. Stewart, J. Q. An inverse distance variation for certain social influences. *Science* **93**, 89–90 (1941).
8. Zipf, G. K. The $p_1 p_2/d$ hypothesis: On the intercity movement of persons. *American Sociological Review* **11**, 677–686 (1946).
9. Roy, J. R. & Thill, J. C. Spatial interaction modelling. *Papers in Regional Science* **83**, 339–361 (2004).
10. Anderson, J. E. The gravity model. *Annual Review of Economics* **3**, 133–160 (2011).
11. Stouffer, S. A. Intervening opportunities: A theory relating mobility and distance. *American Sociological Review* **5**, 845–867 (1940).

12. Schneider, M. Gravity models and trip distribution theory. *Papers in Regional Science* **5**, 51–56 (1959).
13. Simini, F., González, M. C., Maritan, A. & Barabási, A.-L. A universal model for mobility and migration patterns. *Nature* **484**, 96–100 (2012).
14. Song, C., Koren, T., Wang, P. & Barabási, A.-L. Modelling the scaling properties of human mobility. *Nature Physics* **6**, 818–823 (2010).
15. Barbosa, H., de Lima-Neto, F. B., Evsukoff, A. & Menezes, R. The effect of recency to human mobility. *EPJ Data Science* **4**, 21 (2015).
16. Schläpfer, M. *et al.* The universal visitation law of human mobility. *Nature* **593**, 522–527 (2021).
17. Barbosa, H. *et al.* Human mobility: Models and applications. *Physics Reports* **734**, 1–74 (2018).
18. Wang, J., Kong, X., Xia, F. & Sun, L. Urban human mobility: Data-driven modeling and prediction. *ACM SIGKDD Explorations Newsletter* **21**, 1–19 (2019).
19. Pappalardo, L., Manley, E., Sekara, V. & Alessandretti, L. Future directions in human mobility science. *Nature Computational Science* **3**, 588–600 (2023).
20. Cranmer, M. Interpretable machine learning for science with pysr and symbolicregression.jl (2023). Preprint at <https://arxiv.org/abs/2305.01582>.
21. Makke, N. & Chawla, S. Interpretable scientific discovery with symbolic regression: A review. *Artificial Intelligence Review* **57**, 2 (2024).
22. Reichardt, I., Pallarès, J., Sales-Pardo, M. & Guimerà, R. Bayesian machine scientist to compare data collapses for the nikuradse dataset. *Physical Review Letters* **124**, 084503 (2020).
23. Liu, Z. & Tegmark, M. Machine learning hidden symmetries. *Physical Review Letters* **128**, 180201 (2022).

24. Shao, H. *et al.* Finding universal relations in subhalo properties with artificial intelligence. *The Astrophysical Journal* **927**, 85 (2022).
25. Wadekar, D. *et al.* Augmenting astrophysical scaling relations with machine learning: Application to reducing the Sunyaev–Zeldovich flux–mass scatter. *Proceedings of the National Academy of Sciences* **120**, e2202074120 (2023).
26. Weng, B. *et al.* Simple descriptor derived from symbolic regression accelerating the discovery of new perovskite catalysts. *Nature Communications* **11**, 3513 (2020).
27. Li, Y. *et al.* Electron transfer rules of minerals under pressure informed by machine learning. *Nature Communications* **14**, 1815 (2023).
28. Grundner, A., Beucler, T., Gentine, P. & Eyring, V. Data-driven equation discovery of a cloud cover parameterization. *Journal of Advances in Modeling Earth Systems* **16**, e2023MS003763 (2024).
29. Liu, S., Li, Q., Shen, X., Sun, J. & Yang, Z. Automated discovery of symbolic laws governing skill acquisition from naturally occurring data. *Nature Computational Science* **4**, 334–345 (2024).
30. Li, Q. *et al.* Advancing symbolic regression for earth science with a focus on evapotranspiration modeling. *npj Climate and Atmospheric Science* **7**, 321 (2024).
31. Verstyuk, S. & Douglas, M. R. Machine learning the gravity equation for international trade (2022). Preprint at <https://ssrn.com/abstract=4053795>.
32. La Cava, W. *et al.* Contemporary symbolic regression methods and their relative performance. In Vanschoren, J. & Yeung, S. (eds.) *Proceedings of the Neural Information Processing Systems Track on Datasets and Benchmarks*, vol. 1 (2021).
33. Cardoso, P. *et al.* Automated discovery of relationships, models, and principles in ecology. *Frontiers in Ecology and Evolution* **8** (2020).

34. Villaescusa-Navarro, F. *et al.* The CAMELS project: cosmology and astrophysics with machine-learning simulations. *The Astrophysical Journal* **915**, 71 (2021).
35. Lemos, P., Jeffrey, N., Cranmer, M., Ho, S. & Battaglia, P. Rediscovering orbital mechanics with machine learning. *Machine Learning: Science and Technology* **4**, 045002 (2023).
36. Wilson, A. G. *Entropy in Urban and Regional Modelling* (Routledge, London, 1970).
37. Liu, E. & Yan, X. New parameter-free mobility model: Opportunity priority selection model. *Physica A: Statistical Mechanics and its Applications* **526**, 121023 (2019).
38. Lenormand, M., Bassolas, A. & Ramasco, J. J. Systematic comparison of trip distribution laws and models. *Journal of Transport Geography* **51**, 158–169 (2016).
39. Yan, X.-Y., Han, X.-P., Wang, B.-H. & Zhou, T. Diversity of individual mobility patterns and emergence of aggregated scaling laws. *Scientific Reports* **3**, 2678 (2013).
40. Fotheringham, A. S. Spatial structure and distance-decay parameters. *Annals of the Association of American Geographers* **71**, 425–436 (1981).
41. Kwon, O.-H., Hong, I., Jung, W.-S. & Jo, H.-H. Multiple gravity laws for human mobility within cities. *EPJ Data Science* **12**, 57 (2023).
42. Yu, H. Exploring multiscale spatial interactions: Multiscale geographically weighted negative binomial regression. *Annals of the American Association of Geographers* **114**, 574–590 (2024).
43. Fajardo-Fontiveros, O. *et al.* Fundamental limits to learning closed-form mathematical models from data. *Nature Communications* **14**, 1043 (2023).
44. Cranmer, M. *et al.* Discovering symbolic models from deep learning with inductive biases. In Larochelle, H., Ranzato, M., Hadsell, R., Balcan, M. & Lin, H. (eds.) *Advances in Neural Information Processing Systems*, vol. 33, 17429–17442 (2020).

45. Shi, H. *et al.* Learning symbolic models for graph-structured physical mechanism. In *International Conference on Learning Representations* (2023). URL https://openreview.net/forum?id=f2wN4v_2__W.
46. Lenormand, M., Huet, S., Gargiulo, F. & Deffuant, G. A universal model of commuting networks. *PLOS ONE* **7**, 1–7 (2012).
47. Virgolin, M. & Pissis, S. P. Symbolic regression is NP-hard. *Transactions on Machine Learning Research* (2022). URL <https://openreview.net/forum?id=LTiaPxqe2e>.
48. Udrescu, S.-M. & Tegmark, M. AI Feynman: A physics-inspired method for symbolic regression. *Science Advances* **6**, eaay2631 (2020).
49. Udrescu, S.-M. *et al.* AI Feynman 2.0: Pareto-optimal symbolic regression exploiting graph modularity. In Larochelle, H., Ranzato, M., Hadsell, R., Balcan, M. & Lin, H. (eds.) *Advances in Neural Information Processing Systems*, vol. 33, 4860–4871 (2020).
50. Sahoo, S., Lampert, C. & Martius, G. Learning equations for extrapolation and control. In Dy, J. & Krause, A. (eds.) *Proceedings of the 35th International Conference on Machine Learning*, vol. 80 of *Proceedings of Machine Learning Research*, 4442–4450 (2018).
51. Petersen, B. K. *et al.* Deep symbolic regression: Recovering mathematical expressions from data via risk-seeking policy gradients. In *International Conference on Learning Representations* (2021). URL <https://openreview.net/forum?id=m5Qsh0kBQG>.
52. Kamienny, P.-A., d’Ascoli, S., Lample, G. & Charton, F. End-to-end symbolic regression with transformers. In Koyejo, S. *et al.* (eds.) *Advances in Neural Information Processing Systems*, vol. 35, 10269–10281 (2022).
53. Guimerà, R. *et al.* A Bayesian machine scientist to aid in the solution of challenging scientific problems. *Science Advances* **6**, eaav6971 (2020).
54. Jin, Y., Fu, W., Kang, J., Guo, J. & Guo, J. Bayesian symbolic regression (2020). Preprint at <https://arxiv.org/abs/1910.08892>.

55. Koza, J. R. Genetic programming as a means for programming computers by natural selection. *Statistics and Computing* **4**, 87–112 (1994).
56. Schmidt, M. & Lipson, H. Distilling free-form natural laws from experimental data. *Science* **324**, 81–85 (2009).

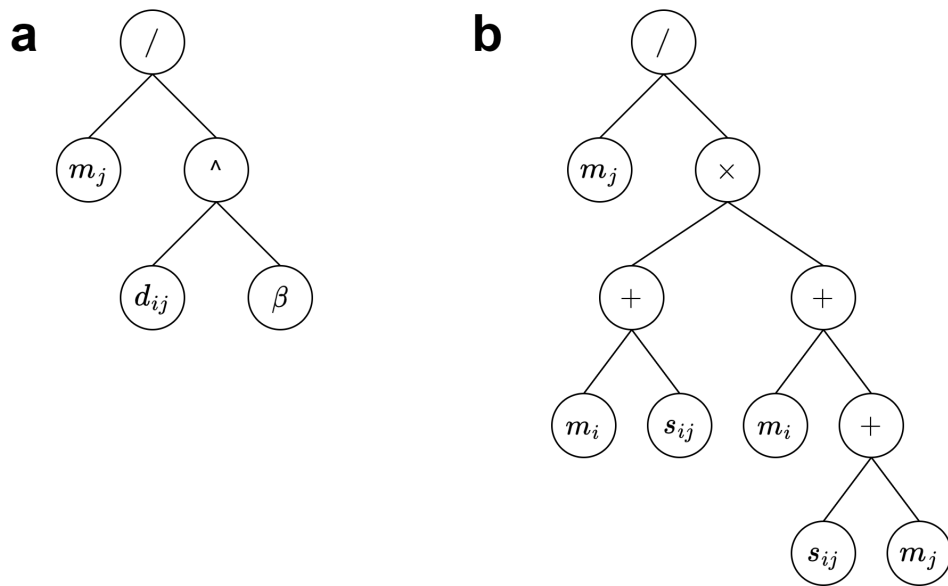
Acknowledgments We acknowledge the support of the National Natural Science Foundation of China under Grant Nos. 42422110 and 42430106. L.D. was supported by the Fundamental Research Funds for the Central Universities, Peking University. We thank Tianyou Cheng and Chengling Tang for assistance in processing the cellphone datasets; Dr. Andre Python, Dr. Ryan Wang, Ce Hou, and Xuechen Wang for helpful discussion.

Author contributions L.D., Y.L., and H.G. conceived the project and designed the experiments; H.G., W.Z., and Y.H. collected the data; H.G., W.Z., and J.Y. performed the experiments; W.Z., and H.G., visualized the results; H.G., L.D., W.Z, and Y.L. wrote the manuscript.

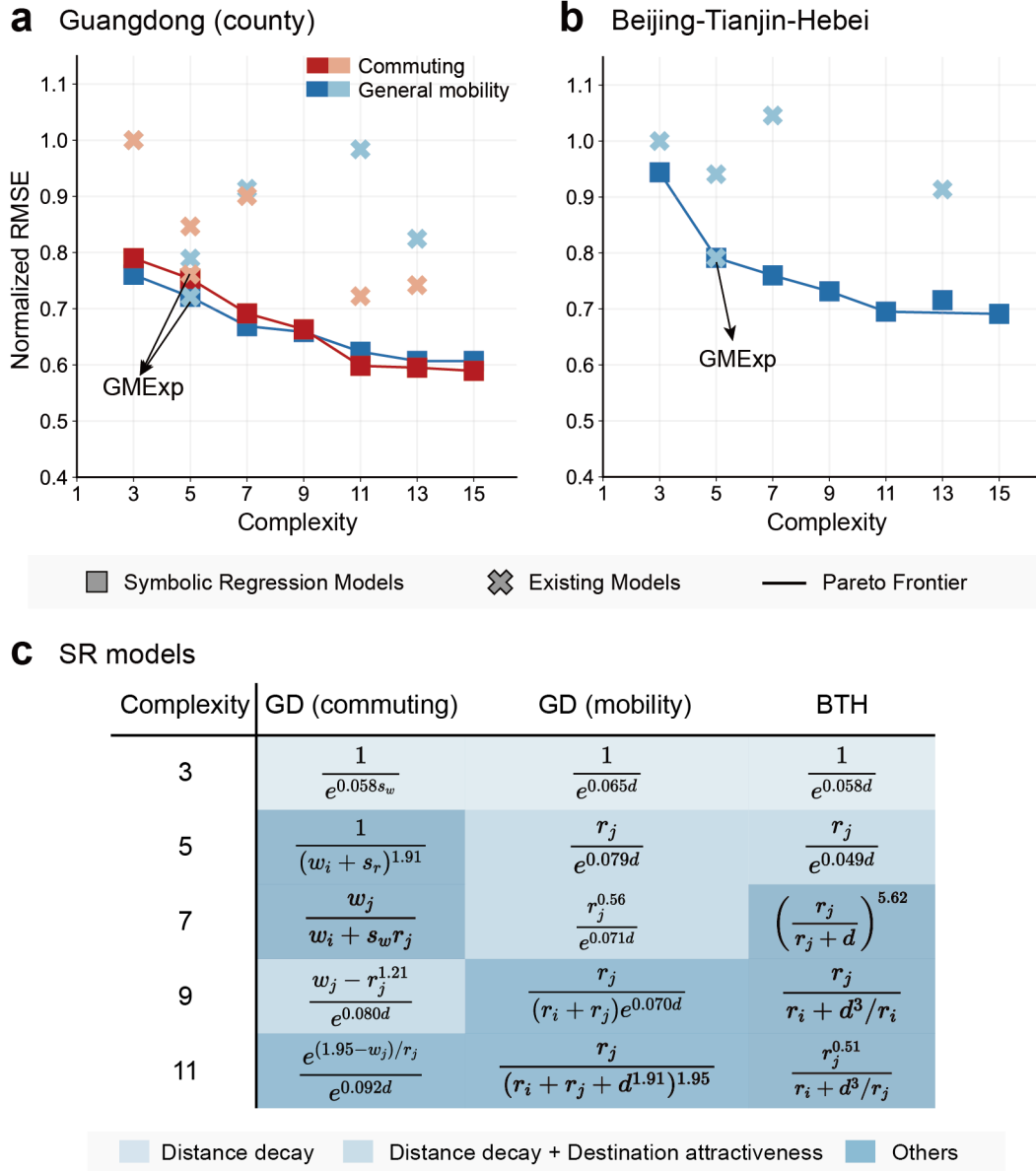
Competing interests The authors declare no competing interests.

Correspondence and requests for materials should be addressed to L.D. or Y.L.

Data and Code Availability All codes and processed flow datasets from the US, the UK, and Beijing-Tianjin-Hebei, China are publicly available on GitHub at <https://github.com/urbansci/FlowSR>. The Guangdong cellphone dataset can be requested from the corresponding authors.



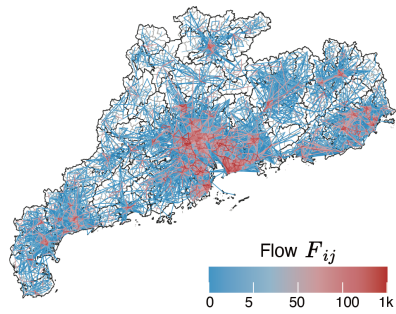
Extended Data Fig. 1: Examples for calculating the model complexity with binary expression trees. (a) Under the allocation weight setting, the gravity model with power-law decay $f_{ij} = m_j/d_{ij}^\beta$ is expressed as a tree with 5 nodes, hence has a complexity of 5. (b) The radiation model $f_{ij} = m_j/(m_i + s_{ij})(m_i + s_{ij} + m_j)$ has a complexity of 11.



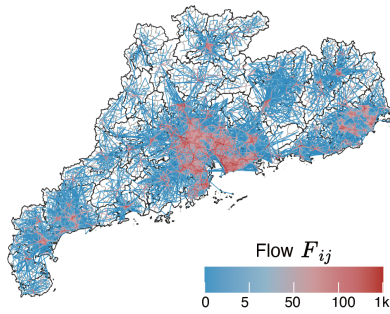
Extended Data Fig. 2: SR results on Guangdong (county level) and Beijing-Tianjin-Hebei (BTH) data. (a-b) Pareto frontiers of SR models on Guangdong and BTH data. As in Fig. 2, the RMSEs are normalized with that of the simplest gravity model (m_j/d_{ij}), and the crosses represent the accuracy and complexity of six existing models (Fig. 2e). (c) Expressions of the Pareto optimal SR models. The notations follow Fig. 1, except that d is short for d_{ij} . The distilled models are classified based on the captured effects governing human mobility. A decay function of intervening opportunity is viewed as a special form of distance decay.

a Guangdong (sub-district)

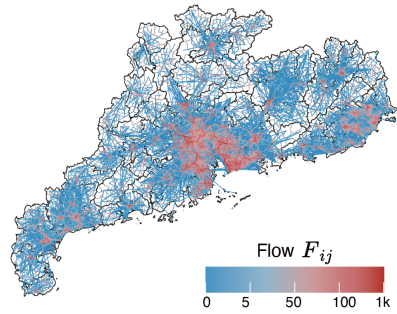
Groundtruth



SR model - complexity 5

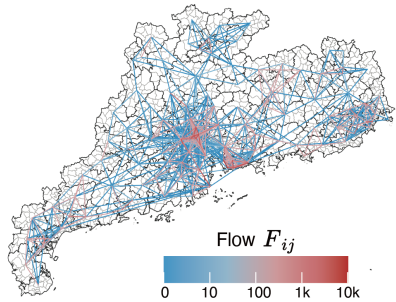


SR model - complexity 7

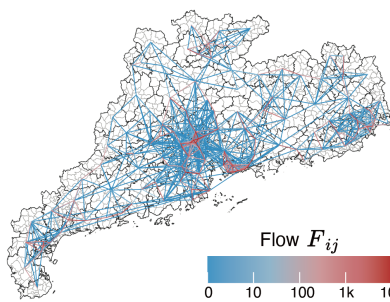


b Guangdong (county)

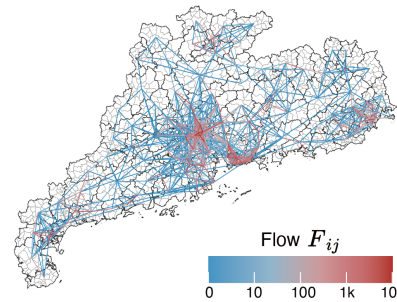
Groundtruth



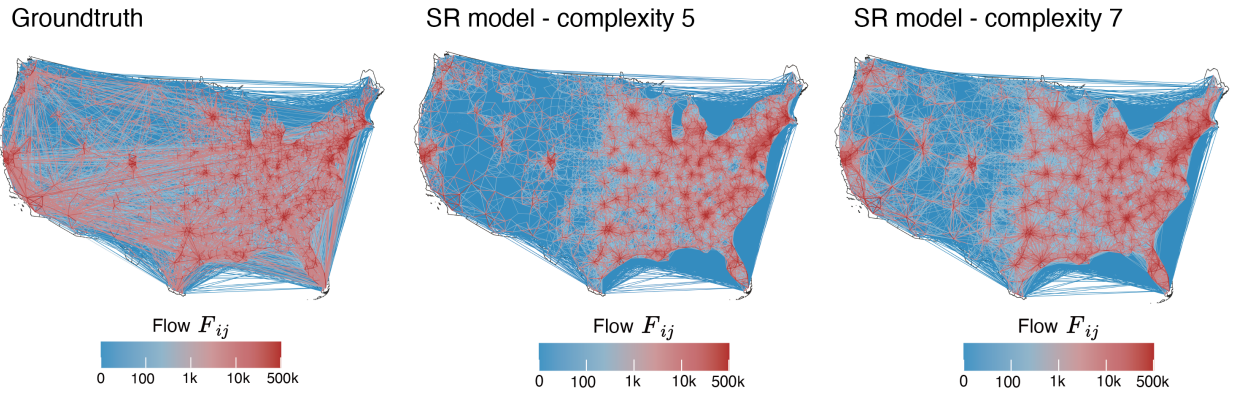
SR model - complexity 5



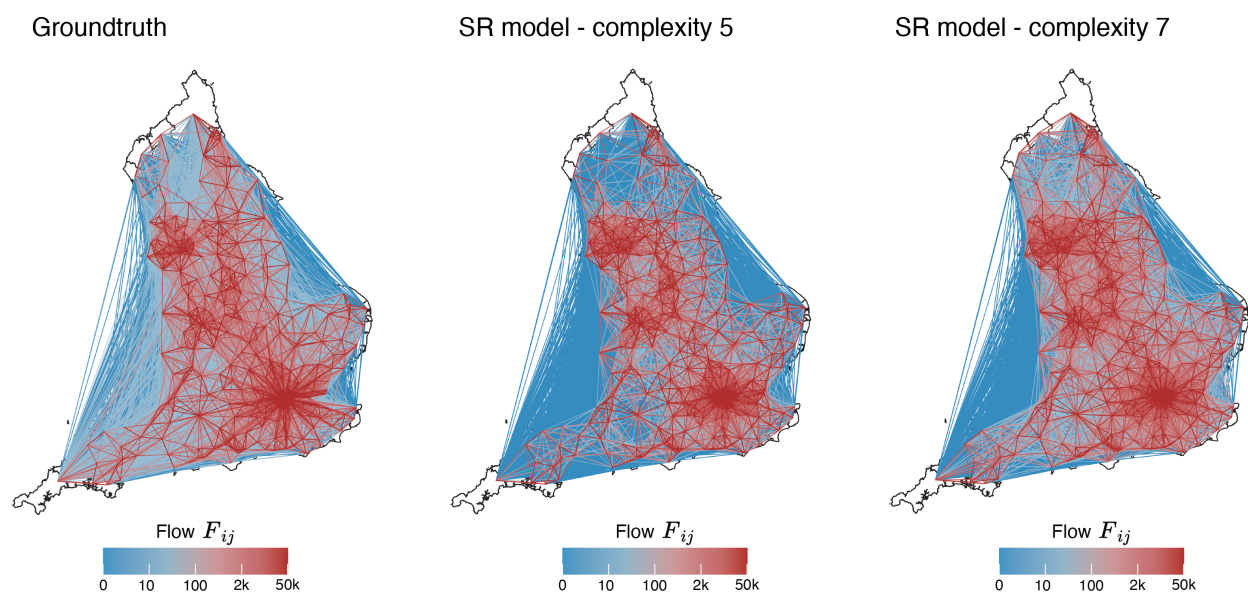
SR model - complexity 7



Extended Data Fig. 3: Actual and SR model-generated commuting flow maps in Guangdong, China, at the (a) sub-district and (b) county levels. SR models with complexity 5 and 7 are used, as SR models at this complexity level exhibit consistent model forms across datasets. These models effectively capture the overall mobility patterns, particularly in estimating flows with high volumes.



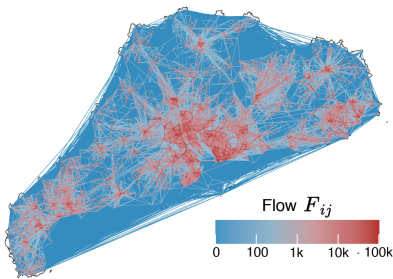
Extended Data Fig. 4: Actual and SR model-generated commuting flow maps in the US. The SR models with complexity 5 and 7 are used.



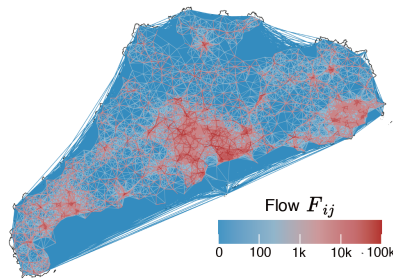
Extended Data Fig. 5: Actual and SR model-generated commuting flow maps in England. The SR models with complexity 5 and 7 are used.

a Guangdong (sub-district)

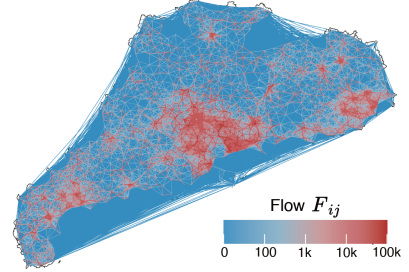
Groundtruth



SR model - complexity 5

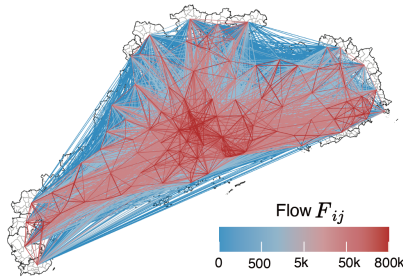


SR model - complexity 7

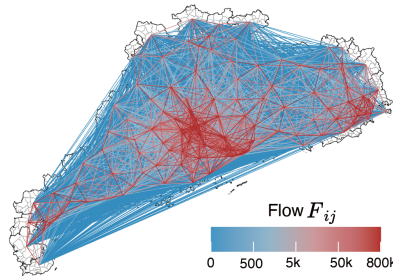


b Guangdong (county)

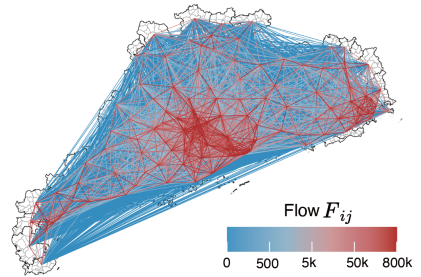
Groundtruth



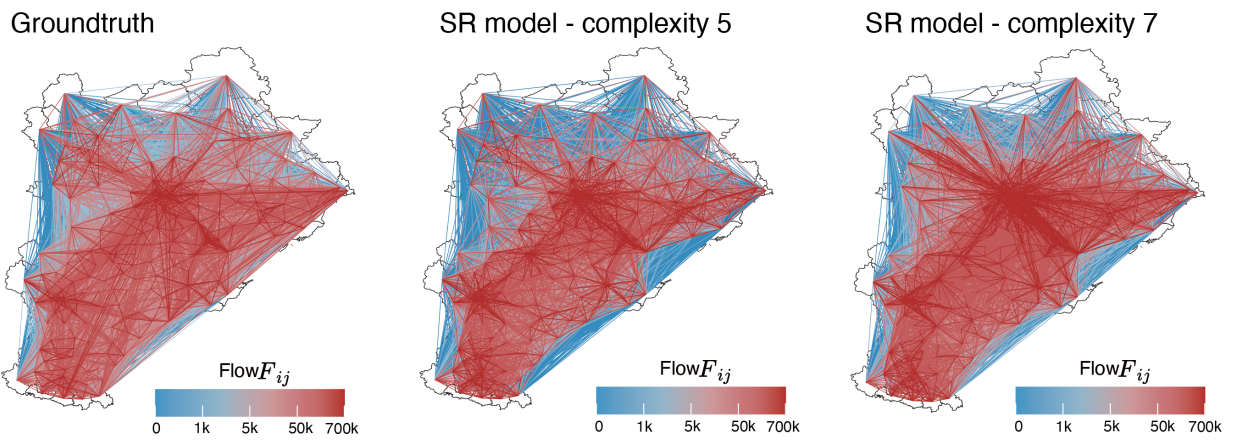
SR model - complexity 5



SR model - complexity 7



Extended Data Fig. 6: Actual and SR model-generated general mobility flow maps in Guangdong, China, at the (a) sub-district and (b) county scale. The SR models with complexity 5 and 7 are used.



Extended Data Fig. 7: Actual and SR model-generated general mobility flow maps in Beijing-Tianjin-Hebei urban agglomeration. The SR models with complexity 5 and 7 are used.

Extended Data Table 1: The accuracy of existing models on flow data, measured by root mean squared error (RMSE). Results on commuting data are based on workplace population, as using residential population yields inferior results. The lowest error on each dataset is put in bold. See Fig. 2e for model definitions. BTH is short for Beijing-Tianjin-Hebei urban agglomeration, China.

Model	Commuting				Mobility		
	Guangdong (sub-district)	Guangdong (county)	England	US	Guangdong (sub-district)	Guangdong (county)	BTH
GMZipf	15.02	146.25	728.58	2105.8	1588.5	12870	81813
GMPow	12.53	123.78	442.23	1338.5	1173.6	11734	76959
GMExp	11.51	111.91	360.34	1309.9	1112.8	10723	64746
RM	22.72	105.62	863.67	2222.4	2023.1	14628	119256
IO	14.20	108.49	587.86	1733.4	1289.8	12260	74732
OPS	12.99	131.69	679.65	2370.0	1332.9	13582	85542

Supplementary Table S1: Description of the real flow datasets. Area and population are median values. MLAD is short for Merged Local Authority District.

Region	Granularity	#Units	Area (km ²)	Population	#Flows
Guangdong	sub-district	2,100	60	36,962	705,811 (mobility) 28,392 (commuting)
Guangdong	county	124	1,256	725,391	14,251 (mobility) 1,150 (commuting)
Beijing-Tianjin-Hebei	county	200	756	440,000	38,813
England	MLAD	324	212	126,430	57,591
US	county	3,108	1,616	25,991	131,391

Supplementary Table S2: SR settings for real data analysis. MLAD is short for Merged Local Authority District. opt means the algorithm for constant optimization. By default, batching is not used, and opt= “BFGS”.

Dataset	Granularity	Explanatory Variables	#Runs	Other Parameters
Guangdong (Commuting)	sub-district	$r_i, r_j, w_i, w_j, d, s_r, s_w$	5	batchsize=40
		w_i, w_j, d	5	
Guangdong (Commuting)	county	$r_i, r_j, w_i, w_j, d, s_r, s_w$	5	
		w_i, w_j, r_j, d	5	
		w_i, w_j, r_j, s_w	5	
England	MLAD	$r_i, r_j, w_i, w_j, d, s_r, s_w$	5	
		w_i, w_j, d	5	
US	county	$r_i, r_j, w_i, w_j, d, s_r, s_w$	5	batchsize=100 opt=“Nelder-Mead”
		w_i, w_j, d	5	
Guangdong (Mobility)	sub-district	r_i, r_j, d, s_r	5	batchsize=40
		r_i, r_j, d	5	
Guangdong (Mobility)	county	r_i, r_j, d, s_r	5	
		r_i, r_j, d	5	
Beijing-Tianjin-Hebei	county	r_i, r_j, d, s_r	5	

Supplementary Table S3: Alternative SR models on Guangdong commuting data. The top 3 distinct expressions on each complexity level are shown. If results across repeated runs are identical, there may be less than 3 expressions to show.

Dataset	Complexity	Expression	RMSE
Guangdong (sub-district)	3	0.79^d	14.68
	5	$w_j/1.24^d$	11.51
	7	$(w_j - r_j)/1.24^d$	11.18
	7	$w_j/\exp(d^{0.56})$	11.41
	9	$w_j^{1.93}/(r_j \cdot 1.24^d)$	11.03
	9	$w_j \cdot w_j/(r_j \cdot 1.24^d)$	11.06
	11	$w_j^2/(r_j \cdot 1.26^d) + d$	10.94
	11	$w_j^2/(r_j \exp(d^{0.57}))$	11.01
	11	$w_j(w_j + 0.025)/(r_j \cdot 1.25^d)$	11.02
Guangdong (county)	3	0.94^{s_w}	115.50
	3	0.93^d	123.85
	5	$(w_i + s_r)^{-1.91}$	110.18
	5	$(w_i + s_w)^{-1.32}$	110.76
	5	$w_j/1.10^d$	111.90
	7	$w_j/(w_i + s_w r_j)$	101.15
	7	$(w_j - r_j)/1.09^d$	104.97
	9	$(w_j - r_j^{1.21})/1.09^d$	97.00
	9	$((w_i + s_w)/w_j + r_j)^{-2.01}$	97.08
	9	$w_j/(1.34^{r_j} \cdot s_w) + w_i$	97.32
	11	$e^{(w_j - b)/r_j}/1.10^d$	87.49
	11	$w_j^2 \cdot (0.6^{w_j})/(1.09^d)$	91.35
	11	$((w_j + s_w)/(w_j - r_i) + r_j)^{-1.80}$	91.77

Supplementary Table S4: Alternative SR models on US commuting data. The top 3 distinct expressions on each complexity level are shown. If results across repeated runs are identical, there may be fewer than 3 expressions to show.

Dataset	Complexity	Expression	RMSE
US	3	w_j/d	2105.8
	5	$w_j/1.04^d$	1309.9
	5	$w_j/d^{2.05}$	1338.5
	7	$w_j/\exp(d^{0.42})$	1188.9
	7	$w_j/(d^{2.28} + r_i)$	1207.9
	7	$w_j/(d^{2.02} + w_i)$	1232.0
	9	$w_j^{1.17}/\exp(d^{0.42})$	1163.3
	9	$w_j/(d^{2.33} + r_i - s_r)$	1167.7
	9	$(w_j/\exp(d^{0.38}))^{1.17}$	1170.1
	11	$a/(\exp(d^{0.41})/w_j - 0.038)$	1135.3
	11	$w_j^{1.18}/(d \cdot (d + w_i)^{2.60})$	1137.1
	11	$w_j/((d \cdot d - w_j) \cdot d + 10279)$	1137.3

Supplementary Table S5: Alternative SR models on England commuting data. The top 3 distinct expressions on each complexity level are shown. If results across repeated runs are identical, there may be fewer than 3 expressions to show.

Dataset	Complexity	Expression	RMSE
England	3	0.89^d	687.10
	5	$w_j/1.11^d$	360.34
	7	$w_j/\exp(d^{0.50})$	343.62
	7	$w_j/(1.09^d - 0.92)$	344.62
	7	$w_j/(d \cdot 1.06^d)$	345.75
	9	$w_j^{1.06}/(1.09^d - 0.94)$	341.02
	9	$(w_j/(1.09^d - 0.89))^{1.04}$	341.41
	9	$((w_j/1.05^d)^{1.07})/d$	341.48
	11	$(10.2w_j - r_j)/(d \cdot 1.06^d)$	336.49
	11	$w_j/((1.06^d)(d + r_j/w_j))$	337.51
	11	$(16.8w_j - r_j)/(1.09^d - 0.95)$	337.54

Supplementary Table S6: Alternative SR models on Guangdong general mobility data. The top 3 distinct expressions on each complexity level are shown. If results across repeated runs are identical, there may be fewer than 3 expressions to show.

Dataset	Complexity	Expression	RMSE
Guangdong (sub-district)	3	0.78^d	1153.2
	5	$r_j/1.24^d$	1112.8
	7	$r_j^{0.55}/1.27^d$	1055.2
	7	$(r_j/1.51^d)^{0.57}$	1055.4
	9	$(r_j/1.58^d + 0.04)^{0.59}$	1038.6
	9	$r_j^{0.54}/1.29^d + 0.07$	1039.3
	9	$(r_j/1.49^d)^{0.67} + 0.4$	1039.6
	11	$(r_j/(1.51^d - 1.03) + 0.04)^{0.59}$	1034.4
	11	$(r_j^{0.54}/1.29^d + 0.13)^{1.05}$	1038.3
	11	$(0.53 \cdot r_j/1.61^d)^{0.55} + 0.06$	1038.5
Guangdong (county)	3	0.93^d	11308.9
	5	$r_j/1.08^d$	10723.1
	7	$r_j^{0.56}/1.07^d$	9948.1
	9	$(r_j/(r_j + r_i))/1.07^d$	9793.8
	11	$r_j/(d^{1.91} + r_j + r_i)^{1.95}$	9271.2
	11	$r_j/(r_i + r_j + d^2)^{1.73}$	9327.8

Supplementary Table S7: Alternative SR models on Beijing-Tianjin-Hebei general mobility data. The top 3 distinct expressions on each complexity level are shown. If results across repeated runs are identical, there may be less than 3 expressions to show.

Dataset	Complexity	Expression	RMSE
Beijing-Tianjin-Hebei	3	0.94^d	77235
	5	$r_j/1.05^d$	64746
	7	$(r_j/(d+r_j))^{5.62}$	62173
	7	$r_j/(d^{1.91}+r_i)$	63173
	7	$(r_j+18.98)/1.05^d$	64033
	9	$r_j/(r_i+d^3/r_i)$	59010
	9	$r_j/\exp(r_i^{-0.63}d)$	59843
	9	$r_j/\exp((d+r_i)^{0.53})$	59883
	11	$r_j^{0.51}/(d^3/r_j+r_i)$	56870
	11	$r_j/(d/(r_i/d)^{1.75}+1.14)$	58777
	11	$(r_j/\exp(r_i^{-0.60}d))^{0.90}$	59643